ISSN 1063-7729, Astronomy Reports, 2019, Vol. 63, No. 5, pp. 391–403. © Pleiades Publishing, Ltd., 2019.
Russian Text © The Author(s), 2019, published in Astronomicheskii Zhurnal, 2019, Vol. 96, No. 5, pp. 393–406.

Anisotropic Scattering of the Radio Emission of the Pulsar B0833−45 in the Vela Supernova Remnant

M. V. Popov[1], A. S. Andrianov[1], M. S. Burgin[1*], V. A. Zuga[1], A. G. Rudnitskii[1], T. V. Smirnova[2], V. A. Soglasnov[1], and E. N. Fadeev[1]

[1]*Astro Space Center, Lebedev Physical Institute, Russian Academy of Sciences, Moscow, 117997 Russia*
[2]*Pushchino Radio Astronomy Observatory, Astro Space Center, Lebedev Physical Institute, Russian Academy of Sciences, Pushchino, Moscow region, 142290 Russia*

Received October 8, 2018; revised November 27, 2018; accepted November 27, 2018

Abstract—Very Long Baseline Interferometry (VLBI) observations of the pulsar B0833−45 have been carried out as part of the scientific program of the RadioAstron mission. Ground support was provided by the Long Baseline Array, which includes radio telescopes in Australia and other countries in the southern hemisphere. The VLBI observations of the pulsar are analyzed in order to derive the parameters characterizing the scattering of the pulsar radio emission: the angular size of the scattering disk, the spatial scale of the diffraction pattern, the drift velocity of this pattern relative to the observer, the pulse scattering time scale, and the characteristic scintillation time and frequency scales, as well as the index of the electron-density fluctuation spectrum. Comparison of these values with the predictions of the theory of scattering on a thin screen enables the determination of the position of the effective screen along the line of sight. Estimates made using various methods give distances to the screen from the observer of 0.79 to 0.87 times the total distance to the pulsar. Although the position of the screen is beyond the boundary of the Vela supernova remnant, this object may play the dominant role in the scattering. The scattering disk is an ellipse with a 2:1 axis ratio and with the inferred position angle of the major axis being $\approx 50°$, based on the changes in the visibility-function amplitude for various orientations of the projected baseline. This conclusion is supported by the shape of the visibility-function amplitude as a function of the delay.

DOI: 10.1134/S1063772919040061

1. INTRODUCTION

The radio emission of pulsars is subject to distortion as it propagates through the interstellar medium, namely, dispersion and scattering on plasma inhomogeneities. The dispersion of radio waves leads to smearing of the pulsar pulses in the receiver bandwidth. Restoration of the true structure of the pulse requires compensation for the dispersion, which is straightforward if the dispersion measure for the pulsar is known [1].

Scattering causes several effects: an increase in angular size, smearing of the pulses, modulation of the radiation intensity (scintillation), and distortion of the radio spectrum. The effects of scattering have a random character. However, statistical parameters, such as the scintillation time scale $t_{\rm dif}$, the time scale for scattering of the pulse $\tau_{\rm sc}$, the decorrelation bandwidth $\Delta f_{\rm dif}$, and the average scattering angle $\theta_{\rm H}$ can be used to study the properties of the scattering inhomogeneities. The values of $\tau_{\rm sc}$, $\Delta f_{\rm dif}$, and $t_{\rm dif}$ can be measured on a single radio telescope by analyzing dynamic spectra, while measurement of the spatial scale of the diffraction pattern $\rho_{\rm dif}$ requires simultaneous measurements of dynamic spectra obtained on two well separated antennas with a baseline comparable to this scale, and $\theta_{\rm H}$ can only be obtained using VLBI observations.

This paper presents the results of VLBI observations of the Vela pulsar carried out as part of the scientific program of the RadioAstron project [2]. This pulsar is located in one of the supernova remnants that is closest to the Sun, born in an explosion that occurred about 11 000 years ago. The parallax distance to the pulsar is 290+20 pc, and the proper motion is $\mu_\alpha \cos\delta = -49.68 \pm 0.06$ mas/yr,[1] $\mu_\delta = +29.9 \pm 0.1$ mas/yr [3]. In this case, the transverse velocity of the pulsar is $V_{\rm psr} = 78 \pm 5$ km/s. A whole complex of objects is located in the direction of the pulsar, including, in addition to the Vela pulsar and supernova remnant, the Gum nebula, a binary system

*E-mail: mburgin@asc.rssi.ru

[1]Milliarcsecond/year.

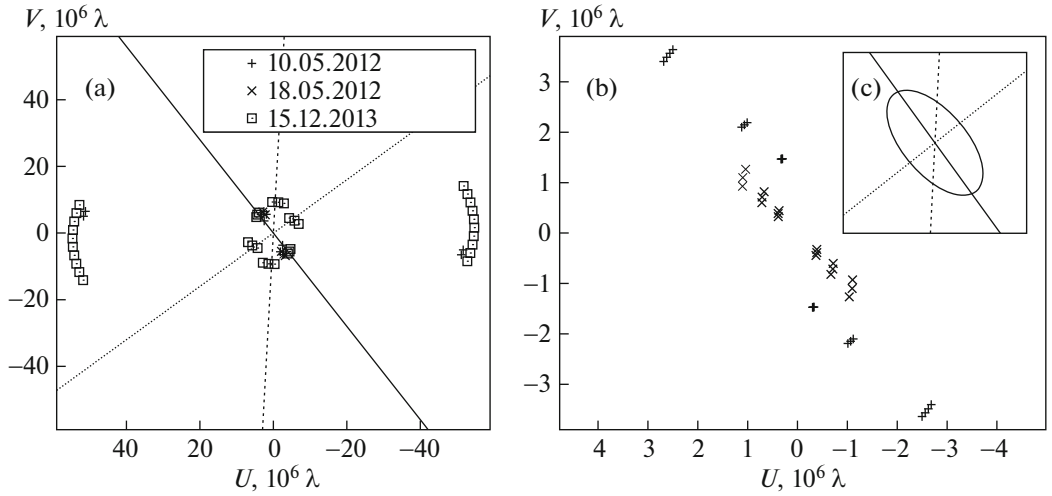

Fig. 1. UV coverage provided by the ground baselines, where the baseline projections are expressed in wavelengths (18 cm). (a) For baseline lengths $>4 \times 10^6\lambda$; the straight lines show the orientation of the baselines used to determine the parameters of the scattering ellipse. (b) For baseline lengths $<4 \times 10^6\lambda$. The inset (c) shows the scattering ellipse on an arbitrary scale.

containing two Wolf–Rayet stars (γ^2 Velorum), the IRAS Vela Shell infrared source, and an OB2 association.

Simultaneous measurement of the size of the scattering disk and the scattering time scale enables estimation of the distance to the effective scattering screen toward the Vela pulsar, in the same way as was done for other pulsars in our earlier studies [4–6].

2. OBSERVATIONS

The observations of B0833–45 were carried out in May 2012 (two sessions) and December 2013 at 1668 MHz. In addition to the RadioAstron space radio telescope (SRT), several radio telescopes of the Long Baseline Array (LBA) took part in the observations, including the Australia Telescope Compact Array (AT) and the Parkes (PA) and Mopra (MP) telescopes in Australia, the Ceduna (CD) and Hobart (HO) telescopes in Tasmania, and the Hartebeesthoek (HH) telescope in South Africa. The NASA Tidbinbilla (TB) radio telescope also participated in one session.

The signal was recorded in a 2×16 MHz band with a central frequency of 1668.0 MHz in left- and right-circular polarizations (LCP and RCP). Two-bit signal digitization was used at the ground telescopes, while one-bit digitization was used for the SRT. Only LCP was recorded at Tidbinbilla. The duration in hours $T_{\rm obs}$ and the set of telescopes participating in each session are given in Table 1.

Table 1. List of observing sessions

Date	$T_{\rm obs}$	Radio telescopes
May 10, 2012	3.0	HH, HO, MP, PA, TB
May 18, 2012	1.5	AT, HH, HO, MP, PA
Dec. 15, 2013	2.5	AT, CD, HH, HO

The data were recorded in scans of 10.5 min and 19.5 min duration for the 2012 and 2013 sessions, respectively, with the data averaged over thirty-second intervals. The automatic gain control system was turned off to avoid triggering on strong pulsar pulses. Due to the inertia of this and the strong change in flux from pulse to pulse, such a trigger would lead to significant data loss.

Figure 1 shows the UV coverage realized by the ground telescopes; to avoid compressing the scale, the ground–space baselines are not shown.

Table 2 shows the approximate sizes of all the baselines in millions of wavelengths. The last column gives the amplitude of the visibility function.

3. MAIN RELATIONS

The response of the interferometer is a function of the mutual coherence of the fields recorded at the radio telescopes at points A and B. This function can be represented in two equivalent forms, namely, in the frequency domain in the form of the complex cross-correlation spectrum,

$$I_{A-B}(f, \mathbf{b}) = \langle E_A(f) \times E_B^*(f) \rangle \,, \qquad (1)$$

where the angular brackets denote averaging in the correlator over a time δ_T, and in the delay domain τ in

Table 2. Projected baseline length $|\mathbf{b}|$ and the visibility-function amplitude $|V(\mathbf{b})|$

Date	Baseline	$\lvert\mathbf{b}\rvert, 10^6\lambda$	$\lvert V(\mathbf{b})\rvert$
May 10, 2012	MP–HO	6.72	0.811(6)
May 10, 2012	TB–HH	52.0	0.09(2)
May 10, 2012	TB–HO	4.35	0.907(3)
May 10, 2012	TB–MP	2.38	0.969(3)
May 10, 2012	TB–PA	1.51	0.983(3)
May 18, 2012	AT–HH	52.2	0.07(2)
May 18, 2012	AT–HO	7.30	0.782(3)
May 18, 2012	AT–MP	0.55	0.986(2)
May 18, 2012	AT–PA	1.51	0.980(3)
May 18, 2012	HO–PA	5.80	0.868(3)
May 18, 2012	MP–HO	6.72	0.75(2)
May 18, 2012	MP–PA	1.0	0.999(4)
May 18, 2012	PA–HH	52.2	0.06(2)
Dec. 15, 2013	AT–CD	6.72	0.87(2)
Dec. 15, 2013	AT–HH	54.5	0.08(2)
Dec. 15, 2013	AT–HO	6.96	0.81(1)
Dec. 15, 2013	HO–CD	9.33	0.89(3)

the form of the complex visibility function V_{AB}, which is related to the intensity I_{AB} as

$$V_{A-B}(\tau, \mathbf{b}) = \mathcal{F}^{-1}(I_{A-B}(f, \mathbf{b})). \qquad (2)$$

Here and below, $\mathbf{b}$ is the baseline vector between the points A and B, and $\mathcal{F}$ denotes a Fourier transform. We did not analyze the phase behavior for these complex functions, and only considered the amplitudes of the visibility function.

The evolution of V_{A-B} and I_{A-B} over time is represented by the dynamic visibility function and dynamic cross-correlation spectrum, respectively. The two-dimensional Fourier transform of the dynamic cross-correlation spectrum gives the so-called secondary dynamic spectrum, or the delay–fringe frequency pattern. Ordered structures such as parabolic arcs are often observed in the secondary dynamic spectra [7]. The autocorrelation and dynamic cross-correlation spectra provide important information regarding the properties of the inhomogeneities causing scattering of the pulsar radiation as it travels to the observer.

The main scattering parameters, such as the scintillation time scale and the decorrelation bandwidth, can be determined from the two-dimensional autocorrelation function of the dynamic spectrum, as was done in [4]. We used a similar method in the present study; however, to suppress the maximum near $\Delta f = 0$, which is mainly due to noise and does not carry useful information, we used the cross-correlation function between the dynamic spectra obtained in the LCP and RCP channels, $DCCF(\Delta f, \Delta t)$, instead of the autocorrelation function.

We determined $|V_{A-B}|$ applying the method described by Shishov et al. [8], which uses the relationship between the modulus of the mean covariance function of the complex cross-correlation spectra and the visibility-function amplitude. As is shown in [8], in the case of strong diffraction scattering, this covariance function can be represented as a sum of two terms, where one depends only on the magnitude of the frequency shift Δf, and the other term depends only on the baseline and gives the value of the spatial coherence function of the field $|B(\mathbf{b})|$.

Thus,

$$J_1(\Delta f) = \left|\left\langle I_{A-B}(f,\mathbf{b}) I^*_{A-B}(f+\Delta f,\mathbf{b})\right\rangle\right| \quad (3)$$
$$= |B(\Delta f)|^2 + |B(\mathbf{b})|^2,$$

where $|B(\Delta f)|^2$ is the frequency correlation function of the flux fluctuations, and $B(\mathbf{b})$ the spatial coherence function of the field normalized to unit flux. As a consequence, the visibility-function amplitude can be determined from the relation

$$\frac{J_1(\mathbf{b}, \Delta f \gg \Delta f_{\text{dif}})}{J_1(\mathbf{b}, \Delta f = 0)} = \frac{|B(\mathbf{b})|^2}{1 + |B(\mathbf{b})|^2}. \quad (4)$$

The use of relation (4) for determining the amplitude of the visibility function is discussed in more detail in [4].

The observed scattering parameters depend on the physical properties and structure of the interstellar plasma. If we analyze our measurements using a simple thin-screen model, according to [9],

$$|B(\mathbf{b})| = \exp\left[-\frac{1}{2}\left(\frac{b}{\rho_{\text{dif}}}\right)^{n-2}\right], \quad (5)$$

where $b = |\mathbf{b}|$ and n is the index in the spectrum of inhomogeneities in the interstellar plasma, which is equal to 4 for a Gaussian distribution and 11/3 for a Kolmogorov distribution.

The spatial diffraction scale ρ_{dif} is related to the scattering angle θ_{sc} as

$$\theta_{\text{sc}} = \frac{\lambda}{2\pi\rho_{\text{dif}}}. \quad (6)$$

In some cases, instead of θ_{sc}, the diameter of the scattering disk θ_{H} is used, which is defined as the Gaussian half-width at half-maximum:

$$\theta_{\text{H}} = 2\sqrt{2\ln 2} \times \theta_{\text{sc}}. \quad (7)$$

The diameter of the scattering disk θ_{H} is included in the relation between the projected baseline length and the visibility-function amplitude as follows [10]:

$$V_{A-B}(b) = \exp\left[-\frac{1}{2}\left(\frac{\pi \times \theta_{\text{H}} \times b}{\sqrt{2\ln 2} \times \lambda}\right)^{n-2}\right]. \quad (8)$$

From the results given in [11], it follows that in the approximation of a thin scattering layer, using the measured scattering time τ_{sc} and the angular size of the scattering disk θ_{H}, we can estimate the distance d_{s} from observer to screen using the relation

$$\frac{d_{\text{s}}}{D} = \left(\frac{\theta_{\text{H}} D}{8c\ln 2 \times \tau_{\text{sc}}} + 1\right)^{-1}, \quad (9)$$

where D is the distance to the pulsar.

The diffraction pattern moves relative to the observer with some effective velocity V_{eff}, which is the result of the vector addition of the velocities of the pulsar $\mathbf{V}_{\text{psr}}$, observer $\mathbf{V}_{\text{obs}}$, and screen $\mathbf{V}_{\text{screen}}$:

$$\mathbf{V}_{\text{eff}} = \frac{d_{\text{s}}}{D - d_{\text{s}}}\mathbf{V}_{\text{psr}} + \mathbf{V}_{\text{obs}} - \frac{D}{D - d_{\text{s}}}\mathbf{V}_{\text{screen}}, \quad (10)$$

and for the scintillation time scale, we shoud have

$$t = \rho_{\text{dif}} / |\mathbf{V}_{\text{eff}}|. \quad (11)$$

We used this relation to determine $\mathbf{V}_{\text{eff}}$ and then d_{s}.

4. DATA REDUCTION

The data were correlated on the correlator of the Astro Space Center (ASC) using dispersion compensation. The correlation was carried out in two ≈ 3 ms windows located on (ON) and outside (OFF) the pulsar pulse. The receiver bandwidth was divided into 8192 frequency channels, which provided a frequency resolution of 1.95 kHz. The ASC correlator produced complex cross-correlation spectra for all combinations of baselines, including autocorrelation spectra. After they were calculated, the individual cross-correlation spectra were averaged over ten pulsar periods. Thus, the cross-correlation spectra at the output of the correlator were formed with an interval of $10P_1$, where $P_1 = 0.089328$ s is the pulsar period.

We analyzed the dynamic autocorrelation spectra $U_{A-A}(f,\mathbf{b},t)$, the individual visibility functions $V_{A-B}(b)$, and the complex covariance functions of the cross-correlation spectra of $J_1(\mathbf{b},\Delta f)$. When constructing the dynamic autocorrelation spectra, a correction was made for the shape of the receiver bandpass for each radio telescope. To do this, the amplitudes of the autocorrelation spectra were averaged for the window outside the pulse (OFF), over the entire 19.5-minute scan. Since the result of such averaging contains noise and interference, we filtered the averaged spectrum via direct and inverse Fourier transform, rejecting high-frequency harmonics before the inverse transform. In practice, 20–30 harmonics were usually retained, depending on the shape of the bandpass for a given telescope. In addition, the bandpass function was reduced to zero at its edges by multiplying it by the function $(1 - \cos(i/n)\pi)/2$, where n is the number of edge points of the spectrum and i is the point number, counted from the edge of the band. In this case, we set $n = 512$, which is exactly 1 MHz. In most cases, these edge zones of the spectrum were not used in the analysis.

Figure 2 shows an example of an averaged spectrum in an LCP channel for the Ceduna radio telescope and the generated amplitude–frequency characteristic of the receiving system $G(f)$. Finally, the difference between the spectra obtained in the ON and OFF windows, normalized to the bandpass shape

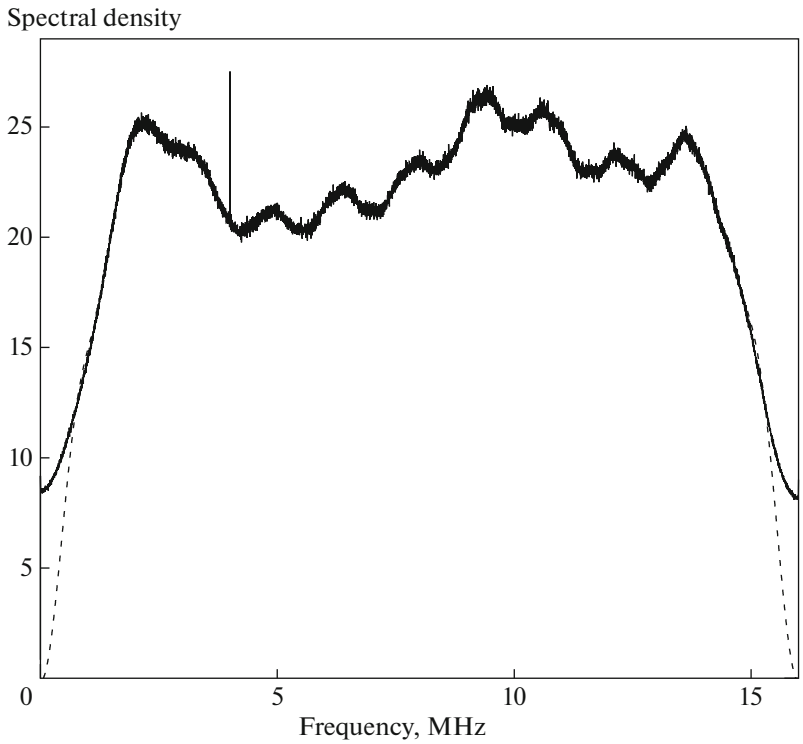

Fig. 2. Amplitude–frequency characteristic of the Ceduna receiver (upper subband, LCP). The solid line shows the mean measured response of the system, and the dashed line the amplitude–frequency characteristic of the system $G(f)$.

$G(f)$, was used as a function of the dynamic autocorrelation spectrum. This subtraction of the individual ON–OFF spectra excludes small-scale dynamic interference. However, in a number of cases, it was necessary to replace zones affected by strong interference with random noise from a previously compiled list of such regions.

Another value used in our analysis is the amplitude of the visibility function $V_{A-B}(\tau, b)$. This was calculated via the inverse Fourier transform of the complex cross-correlation spectra $U_{A-B}(f, \mathbf{b})$, which was obtained at the correlator output. We analyzed the individual visibility functions, since averaging over 10 pulses had already been carried out in the correlator. The Vela pulsar is the brightest pulsar in the sky, which, with the averaging indicated, provides good signal-to-noise ratios for determining the maximum visibility-function amplitude.

In determining the maximum visibility-function amplitude $V_{A-B}(\tau, b)$, we used the mean covariance function of the individual cross-correlation spectra $J_1(\Delta f)$. In this case, the averaging was carried out in complex form, and only in the end was the amplitude of the covariance function calculated.

5. DYNAMIC SPECTRUM AND STRUCTURE FUNCTION

The dynamic spectrum obtained for one scan on the AT in the RCP channel on Dec. 15, 2013 is shown in Fig. 3a. The two-dimensional correlation function $DCCF(\Delta f, \Delta t)$ between the dynamic spectra obtained in LCP and RCP for the same scan is shown in Fig. 3b.

Figure 4 shows cross sections of this function in time and frequency. In the frequency section, two scales were identified, and the function $DCCF(\Delta f, 0)$ was approximated by the expression

$$DCCF(\Delta f, 0) = a_1 \exp(-|\Delta f|/b_1) + a_2 \exp(-|\Delta f|/b_2), \quad (12)$$

where $b_1 = 9.1$ kHz and $b_2 = 47.8$ kHz.

The time cross section was approximated by a Gaussian with a half-width at the $1/e$ level of 9.0 s. Thus, our frequency resolution is a factor of three smaller than the decorrelation band, and the time resolution is an order of magnitude shorter than the scintillation time scale.

Structure functions can be obtained from the $DCCF$ sections shown in Figs. 4a and 4b:

$$DS(\Delta f) = 2.0(DCCF(0,0) - DCCF(\Delta f, 0)), \quad (13)$$

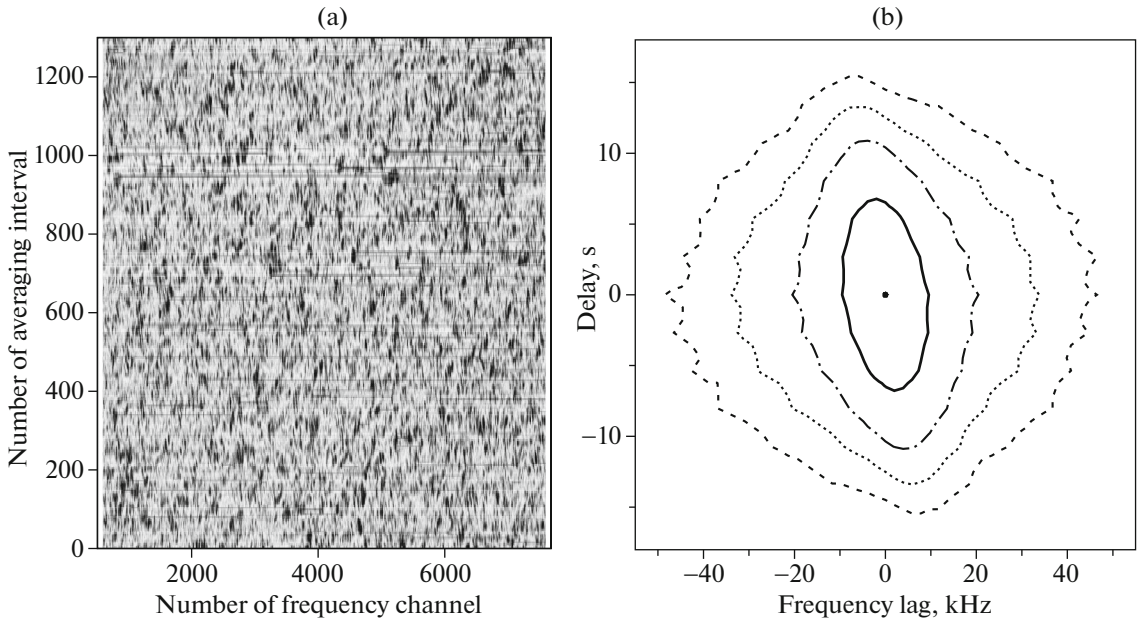

Fig. 3. (a) Dynamic spectrum for one scan obtained on Dec. 15, 2013 with the AT in the LCP channel and (b) cross-correlation between the dynamic spectra obtained with the AT in the LCP an RCP channels. Contours correspond to levels of 0.05, 0.1, 0.2, and 0.5 of the maximum value.

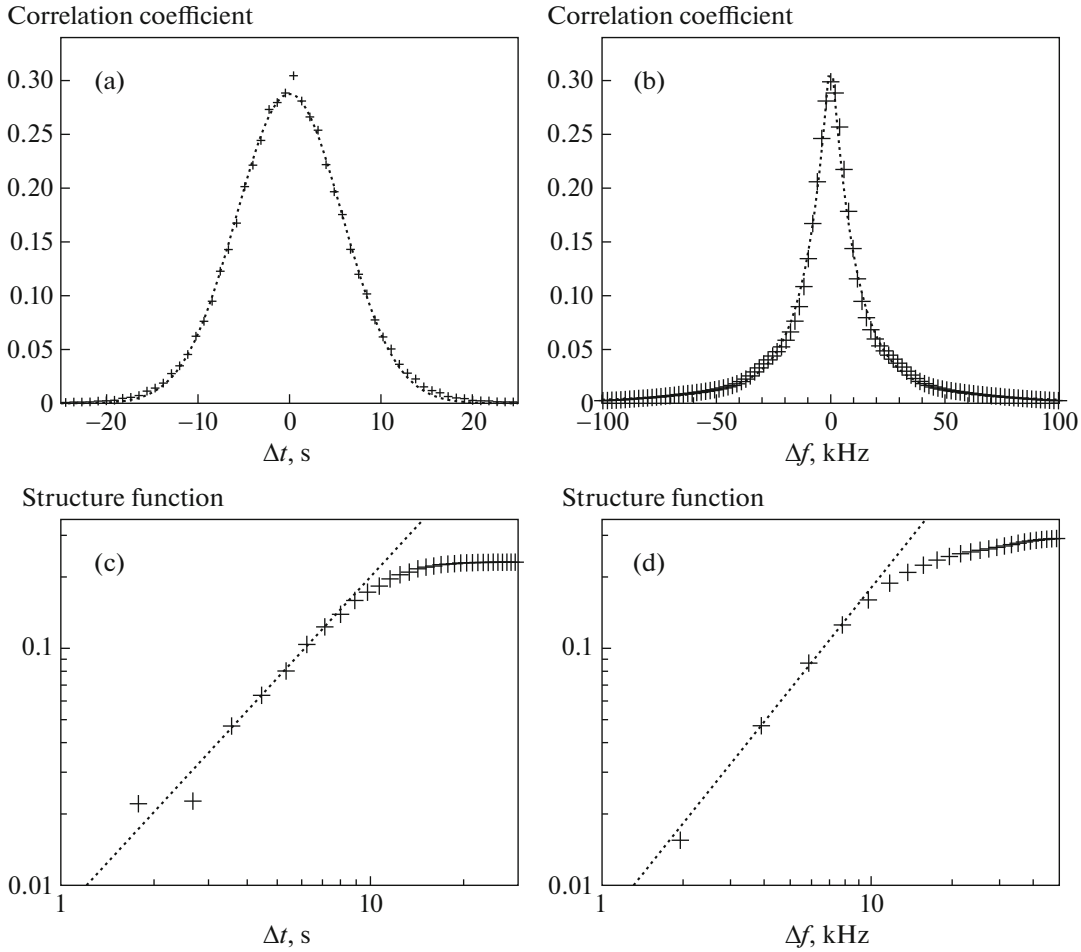

Fig. 4. 2013 observing session. Cross sections of the two-dimensional correlation function and structure function in time (a, c) and frequency (b, d). The dashed lines in panels (c) and (d) show the best power-law fits for the initial parts of the corresponding structural functions.

Table 3. Table of measured parameters

Date	$\Delta f_{\text{dif}}^{(1)}$, kHz	$\Delta f_{\text{dif}}^{(2)}$, kHz	t_{dif}, s	$\tau_{\text{sc}}^{(1)}$, μs	$\tau_{\text{sc}}^{(2)}$, μs	θ_{H}, mas	n_t	n_f
May 10, 2012	8.4(5)	28(3)	6.4(3)	6.3(3)	19.0(3)	6.4(4)	1.48(9)	0.98(2)
May 18, 2012	7.3(1)		6.2(1)	9.2(1)		6.4(4)	1.6 (1)	0.99(3)
Dec. 15, 2013	6.2(2)	33(3)	9.0(3)	3.6(3)	21.5(5)	8.0(3) × 3.6(2)	1.42(4)	1.42(6)

$$DS(\Delta t) = 2.0(DCCF(0,0) - DCCF(0,\Delta t)). \quad (14)$$

These functions are presented in Figs. 4c and 4d on a log–log scale. As was shown by Shishov et al. [12], the slope of the initial part of the temporal structure function α is related to the exponent in the distribution of plasma inhomogeneities $n = \alpha + 2$. Our measured slope α of the temporal structure function $DS(\Delta t)$ for the 2013 observations turned out to be 1.42 ± 0.04, which corresponds to an exponent in the power-law inhomogeneity spectrum of 3.42. Interestingly, the slope of the initial segment of the frequency structure function $DS(\Delta f)$ is also 1.42 ± 0.06. For epoch 2012, the exponent α in the temporal structure function retains a value of about 1.5, and the exponent in the frequency structure function differs from the 2013 value and is close to one. All our measured scattering parameters are given in Table 3.

According to the two-dimensional $DCCF(\Delta f, \Delta t)$ for the 2013 observations (Fig. 3b), the frequency drift of the diffraction structure of the dynamic spectrum is appreciable. The measured drift velocity is 5.2 kHz/s. The presence of such a drift, as well as the similar slopes of the frequency and time structure functions, indicate that the formation of the frequency–time structure of the scintillations is significantly affected by refraction due to a "cosmic prism" located between the observer and the pulsar. Similar effects have been found when observing other pulsars [4, 12, 13].

Since the projection of the AT–HH baseline on the velocity vector of the diffraction pattern is fairly large (its maximum value is 9100 km), we were able to reliably measure the time delay of the scintillation pattern using the two-dimensional correlation of the dynamic spectra obtained at these stations. In this case, we used the delay values averaged for the LCP and RCP receiver channels.

Figure 5a shows an example of a $DCCF$ delay section for epoch 2013. Because of the change in the orientation of the baseline due to the daily rotation of the Earth, the time delay changed significantly during the observations. The measured delay is shown in Fig. 5b. The total amplitude of the sinusoidal curve was 16.8 ± 2.2 s. The drift speed of the diffraction pattern is 540 ± 60 km/s. The corresponding fitted sine curve is shown by the solid curve, and the dashed line corresponds to a speed of 340 km/s, determined in the next section using the values of ρ_{dif} and t_{dif}.

As indicated above, the pulsar's own transverse speed is 78 ± 5 km/s. Assuming $V_{\text{screen}}, V_{\text{obs}} \ll V_{\text{psr}}$, Eq. (10) yields a distance from the observer to the screen of 0.87 ± 0.10 in units of the total distance to pulsar. We used this method for estimating the distance to the scattering screen earlier in [4, 8, 9].

6. VISIBILITY-FUNCTION AMPLITUDE AND SCATTERING SCREEN POSITION

To measure the scattering angle, we used the dependence of the visibility-function amplitude on the baseline length. The visibility-function amplitude can be obtained by normalizing the "raw" values output by the correlator using a correction factor that takes into account the real contribution of the pulsar radiation to the total signal received at each radio telescope. However, this normalization is not trustworthy, due to the non-optimal gain of the receiving system at the pulsar pulse when the automatic gain control is turned off. Therefore, we used another method that does not depend on normalization of the visibility function.

The visibility-function amplitude can be obtained by comparing the cross-correlation spectrum covariance function at its maximum at $\Delta f = 0$ with a value beyond the limit of the decorrelation bandwidth ($\Delta f \gg \Delta f_{\text{dif}}$) using relation (4). Figure 6 illustrates this method, and shows the dependences of the covariance function on the frequency shift for the AT–CD and AT–HH baselines for epoch 2013.

The visibility-function amplitude measured on the AT–HH baseline (with a length of 9720 km) is 0.077. Based on these values, using Eq. (5), and taking the index for the ditribution of inhomogeneities to be $n = 3.42$, we obtain the spatial scale of the diffraction pattern $\rho_{\text{dif}} = 3070 \pm 200$ km and $\theta_{\text{sc}} = 1.9 \pm 0.2$ mas ($\theta_{\text{H}} = 4.5 \pm 0.3$ mas). Assuming that the pulsar velocity is substantially greater than the velocities of

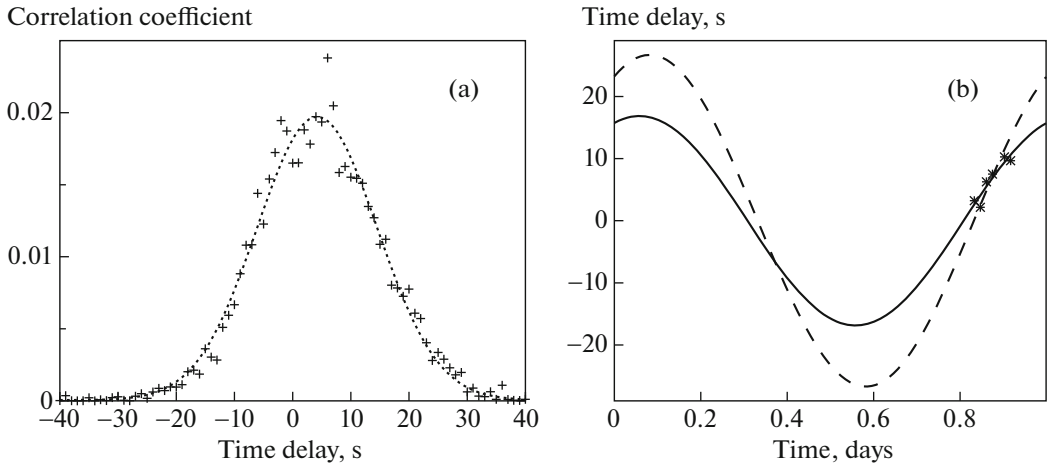

Fig. 5. (a) Determination of the time delay between the dynamic spectra obtained on the AT–HH baseline for the 2013 observation session and (b) the dependence of this time delay on the time of day. The solid curve shows the fitted sinusoid, and the dashed line corresponds to a speed of 340 km/s.

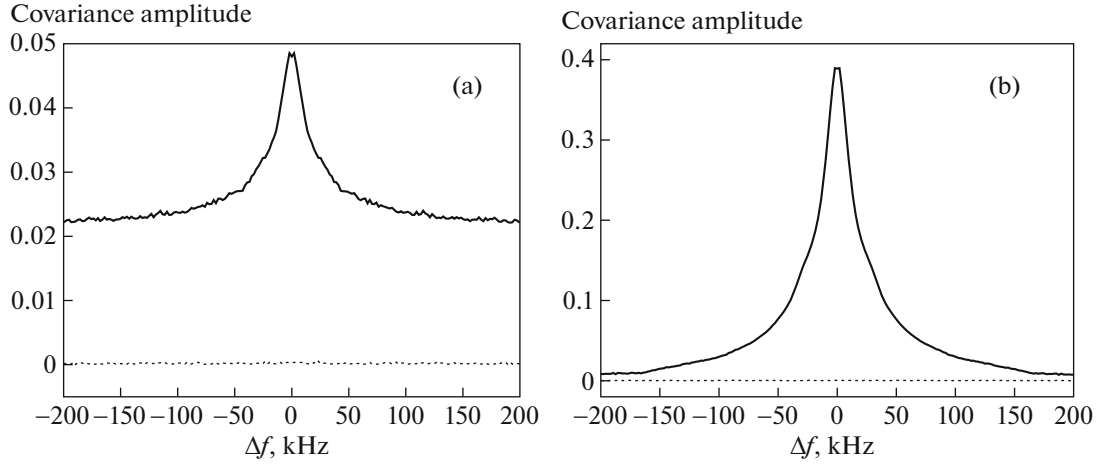

Fig. 6. Covariance functions of cross-correlation spectra on the (a) AT–CD and (b) AT–HH baselines for epoch December 2013. The dashed curve shows the covariance obtained from measurements outside the pulsar pulse.

the observer and the screen, we can find the effective speed of the diffraction pattern relative to the observer and the distance to the screen (see Eq. (10)): $V_{\rm eff} = \rho_{\rm dif}/t_{\rm dif} = 340 \pm 30$ km/s and $d_{\rm s}/D = 0.81 \pm 0.08$. Here we used the pulsar velocity $V_{\rm psr} = 78 \pm 5$ km/s [3] and $t_{\rm dif} = 9$ s. The obtained value of $d_{\rm s}/D$ coincides with the value obtained by Desai et al. [14] within the uncertainties.

The measured value of $V_{\rm eff}$ due to the delay of the diffraction pattern on the AT–HH baselin (540 km/s) is a factor of 1.6 larger than is indicated above. For $V_{\rm eff} = 340$ km/s, a time lag of 26.5 s should be expected, and the corresponding sinusoid is shown by the dash-dotted curve in Fig. 5b, which fits the experimental data well.

Finally, we estimated the position of the effective scattering screen using (9). We adopted the scattering angle determined above on the AT–HH baseline (4.5 mas). To determine the scattering time scale, we calculated the inverse Fourier transform of the dynamic cross-correlation spectrum and averaged its amplitude over time. This corresponds to the visibility function and is shown in Fig. 7. For $\tau_{\rm sc}$, we used the value corresponding to the half-maximum of the function shown in Fig. 7, 10 ± 1 μs. This yields the value 0.79 ± 0.05 for the ratio $d_{\rm s}/D$; the relatively large uncertainty is associated with some arbitrariness in the choice of the $\theta_{\rm H}$ and $\tau_{\rm sc}$ values for an elliptical scattering disk.

7. SIZE, SHAPE, AND ORIENTATION OF THE SCATTERING DISK

For the simplest model with a thin scattering screen in which the inhomogeneities are due to

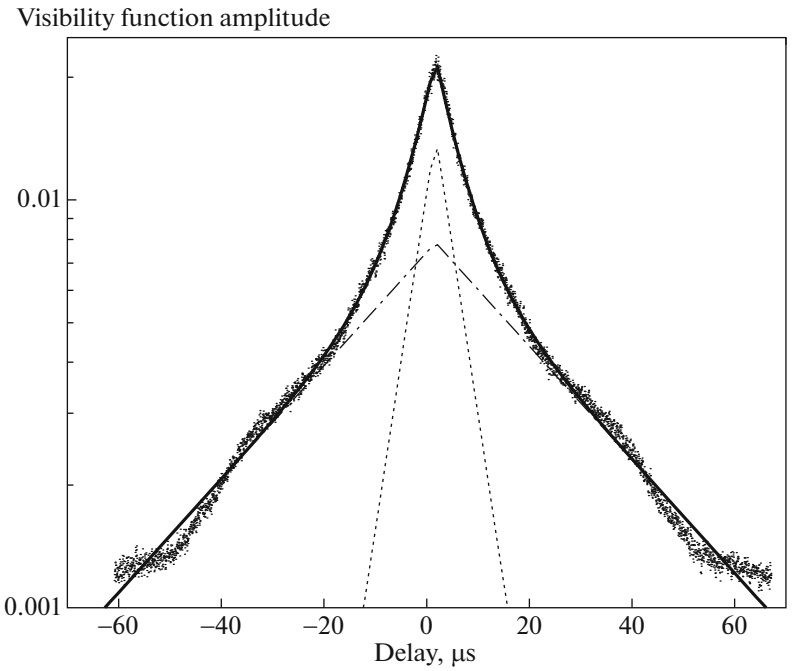

Fig. 7. Dependence of the visibility-function amplitude on the AT–HH baseline on the delay, averaged over the entire interval of the 2013 observations. The dashed and dash-dotted curves show the individual terms in the fit as a sum of two exponentially decreasing components.

isotropic turbulence with a power-law or Gaussian spectrum, the brightness distribution over the scattering disk is axially symmetric. The spatial coherence function $|B(\mathbf{b})|$ does not depend on the orientation of the baseline $\mathbf{b}$, and is a decreasing function of the baseline length $|\mathbf{b}|$ (see Eq. (5)). Accordingly, the parameter $\theta_{\rm H}$ is uniquely determined by the model and does not depend on the baseline orientation.

A preliminary analysis of the observations showed that this simple model is incompatible with our data, whose interpretation requires a more complex model in which the brightness distribution of the scattered radiation is not axially symmetric, and $|B(\mathbf{b})|$ depends not only on $|\mathbf{b}|$, but also on the orientation of the vector $\mathbf{b}$. As such a model, we used a two-dimensional Gaussian brightness distribution for the scattered radiation in the plane of the sky. In this approximation, $\theta_{\rm H}$ depends on the baseline orientation, since the contours of the scattered radiation are similar ellipses with collinear major axes. The model is uniquely characterized by three parameters: the major and minor axes of these contours at a specified level (for which we used the half-maximum level) and the position angle of the major axis.

Figure 8 shows the visibility-function amplitude obtained from observational data using (4) and theoretical fits obtained using the dependence (8) for the data used to determine the shape of the scattering disk. The left and right panels show all the measurements for the 2012 and 2013 observations, respectively. Since the distances between the AT, CD, and HO stations are significantly less than the distance between the Australian stations and the HH station in South Africa, the differences between the results obtained on the AT–HH, CD–HH, and HO–HH baselines are small and comparable with the uncertainties. For this reason, the data obtained on these three baselines were considered together during the post-correlation processing and analysis.

To determine the shape of the scattering disk, the radii of the disk were calculated separately for baselines with different position angles. Only baselines with lengths of $< 10^7\lambda$ were used, that is, only measurements obtained on the Australian baselines. This was done in order to eliminate possible distortion of the results by substructure in the scattering disk, similar to that found in the observations of PSR B0329+54 in [15]. This substructure is not resolved on small baselines, and so does not affect the measurement results. With an increase in the baseline length, however, the presence of substructure results in a decrease in the visibility function. This effect is not taken into account when using a simple model with an elliptical Gaussian scattering disk, and can lead to large errors.

The Australian baselines observed in 2012 are all oriented approximately in one direction. As can be

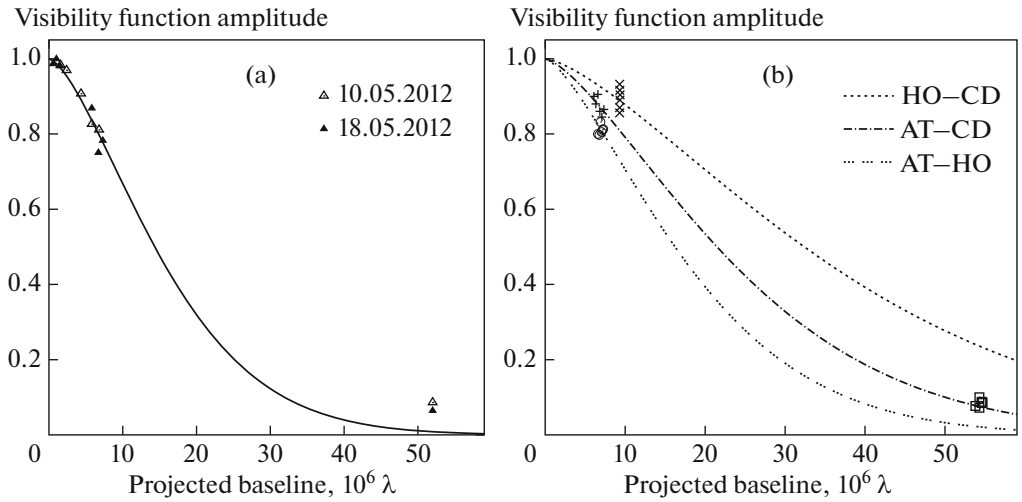

Fig. 8. Dependence of the visibility-function amplitude on the baseline for the (a) 2012 and (b) 2013 observations. The measured values for the HO–CD, AT–CD, AT–HO, and AT–HH baselines are shown by the symbols ×, +, ⊙, and ⊡.

seen from Fig. 8a, for these baselines, the measured visibility-function amplitudes are well fitted by the dependence (8) with $n = 1.5$ and the scattering angle $\theta_{\rm H} = 6.5$ mas.

Figure 8 shows a significant scatter for the visibility-function amplitudes measured in 2013, which we associate with differences in the baseline orientations. We obtained separate fits for various baselines: AT–HO, AT–CD, and HO–CD. The fitted curves for these baselines are shown in Fig. 8b. As a result, we obtained for the measured diameters of the scattering ellipse $\theta_{\rm H}$(AT–HO) = 8.0 mas, $\theta_{\rm H}$(HO–CD) = 3.8 mas, and $\theta_{\rm H}$(AT–CD) = 4.5 mas.

Figure 1 shows that the AT–CD, AT–HO, and HO–CD baselines have position angles that differ from each other by 40° or more, making it possible to uniquely identify the three parameters of the scattering ellipse from the three measured values $\theta_{\rm H}$. Our measurements correspond to an elliptical scattering disk with axial ratio ≈2 : 1 and the position angle of the major axis 50° ± 20°.

Another approach to determining the scattering indicatrix is based on measuring the delay of an observed pulsar pulse due to the difference in the geometric paths traversed by the radiation that crosses the screen at different points in the scattering disk. The dependence of the amplitude of the averaged visibility function on the delay for an elliptical Gaussian scattering disk was considered by Gwinn et al. [15, Appendix C]. That study shows that, for the model we used, two exponential decay scales for the pulse should be observed in the pulse transfer function. The ratio of these scales is determined by the ratio of the minor and major axes of the scattering ellipse. For an axisymmetric indicatrix, when the ellipse degenerates into a circle, these two scales become equal, and the decay is described by a simple exponential function.

Figure 7 shows the measured dependence of the visibility-function amplitude $V_{\rm AT-HH}(\tau)$ on the delay τ obtained after averaging over the entire observation interval on December 15, 2013. The observed attenuation cannot be described by an exponential function, as would be expected for axisymmetric scattering. To determine the two scales characterizing the shape of the elliptical scattering disk, the visibility-function amplitude was fitted using a function similar to (12), yielding the following values for the parameters characterizing the pulse delay due to the scattering: $\tau_{\rm sc}^{(1)} = 3.6 \pm 0.3$ μs and $\tau_{\rm sc}^{(2)} = 21.5 \pm 0.5$ μs.

The measured scattering parameters for other observing sessions are given in Table 3. The values of $\Delta f_{\rm dif}$ and $\tau_{\rm sc}$ are given at the half-maximum level and the values of $t_{\rm dif}$ at the $1/e$ level. The rms uncertainty in the last digit is shown in parentheses. In the observing session on May 18, 2012, there is only one exponential scale for the decorrelation bandwidth in the spectrum, and only one exponential scale in the dependence of the amplitude of the mean visibility function on the delay.

Another possible indicator of ellipticity of the scattering indicatrix is parabolic arcs, which may occur in the secondary spectra of scattered radiation in certain cases. The secondary spectrum corresponding to the dynamic spectrum of Fig. 3a is shown in Fig. 9. There were no signatures of parabolic arcs in the secondary spectra for this or any other of our observations.

Cordes et al. [16] computed secondary spectra for elliptical scattering disks with various eccentricities and orientations with respect to the direction of the

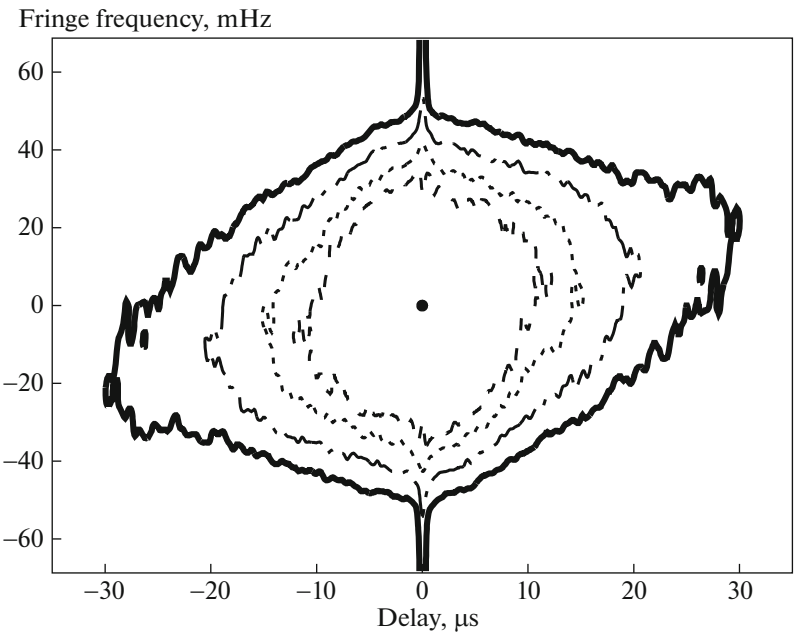

Fig. 9. Secondary spectrum corresponding to the dynamic spectrum shown in Fig. 3a. The contours correspond to 10^{-5}, 10^{-3}, 0.1, and 0.5 of the maximum value.

drift of the diffraction pattern. Our measured parameters are close to those corresponding to [16, Fig. 5d] (axial ratio 3:1, with the vector $V_{\rm eff}$ directed along the minor axis), and the shape of the secondary spectrum we measured is qualitatively consistent with the results of model computations from [16].

8. DISCUSSION

The above results show that determining the distance to the scattering layer using different methods gives different results, which can naturally be interpreted as reflecting the presence of more than one scattering screen along the line of sight. The presence of several screens is not in itself unusual, and this was inferred earlier for the pulsars B0834+06 [4], B1919+21 [8], B1933+16 [5], and the Crab Nebula pulsar B0531+21 [6]. By analogy with the Crab Nebula pulsar, where one of the scattering screens is associated with the boundary layer between the supernova envelope and the surrounding interstellar medium, it may be assumed that a turbulent plasma near the boundary of the Vela supernova remnant is responsible for the formation of the scattering layer closest to the pulsar.

However, our localization of this layer is not in good agreement with the value derived from X-ray observations of $R_{\rm NE}$, the radius of the northeast sector of the supernova remnant onto which the pulsar is projected. According to [17], $R_{\rm NE} = 18$ pc, which corresponds to $d/D = 0.94$ for a distance to the pulsar of $D = 290$ pc, which lies outside the distance from the observer to the screen, consistent with measurements of the drift velocity of the scintillation pattern. One possible reason for this contradiction is that the approximation we used does not provide an adequate description of the scattering of radiation on plasma inhomogeneities inside the supernova remnant.

The main difficulty is that taking into account additional scattering outside the main thin scattering screen leads to a shift in the best-fit position of the screen farther away from the observer. For B0833−45, there are two regions of the interstellar medium that can significantly affect the statistical properties of the scattered radio emission and thus distort interpretation of the observations: the Gum nebula and the background interstellar medium along the line of sight between the Sun and the pulsar.

The Gum Nebula is a large region of ionized gas, inside which the Vela supernova and γ^2 Velorum are located. Reynolds [18] estimated the emission measures in two directions close to the pulsar based on Hα observations, and obtained a shell thickness with an enhanced electron concentration $L = {\rm DM}^2/{\rm EM} = 15{-}30$ pc and $n_e = {\rm EM}/{\rm DM} = (2.5{-}5)$ cm^{-3}. Parcel [19] modeled the outer shell of the nebula as a spherical shell of ionized gas expanding into the ambient environment, and obtained the shell thickness $L = (18.5 \pm 1.5)$ pc, in good agreement with the result of Reynolds [18]. The dispersion

measure of the pulsar is DM = 69.08 pc/cm^3, corresponding to $n_e = 3.7$ cm^{-3} with a screen thickness of 18.5 pc. This number density is a factor of 100 the value outside the shell, and almost all the dispersion measure is concentrated here. According to [20], the scattering angle and scatter broadening of pulses of B0833−45 can be explained by the influence of the turbulent medium in the Gum Nebula shell.

The effect of additional sources of scatterering on the interpretations of observations in models with a single thin screen was studied in [14]. Without taking into account additional sources of scatterering, the best agreement with the observations was achieved with $d_s/D = 0.81 \pm 0.03$, but an admixture of a turbulent plasma uniformly distributed along the line of sight with parameters corresponding to those of the Galactic disk leads to $d_s/D = 0.87$. If we assume that the main source of additional scattering is the Gum Nebula, and its contribution is 5% of the scattering in the main thin layer of the model, the revised distance estimate becomes $d_s/D = 0.96$.

Thus, it seems very likely that the distance estimates we have obtained in the thin-screen model are lower limits, and that the region inside the supernova remnant makes a significant contribution to the scattering.

According to [17], the structure of the Vela supernova remnant can be described by the model proposed in [21], in which the shell is expanding in a two-phase interstellar medium consisting of clouds and intercloud medium. In this model, the initial shock propagates through a hotter and more rarefied intercloud medium, and relatively cool and dense clouds can continue to exist for a long time in the inner regions of the shell. At the same time there is heating and "evaporation" of the clouds near the interface between the two phases due to thermal conduction, leading to a decrease in the mass fraction of the cloudy phase with time. If the density contrast between the clouds and the intercloud medium is high, the velocity acquired by a cloud after the passage of the shock is low compared to the plasma flow velocity of the intercloud medium. Further, due to hydrodynamical interactions between the cloud and the intercloud gas flowing around it, the velocities of the two phases become equalized.

The boundary between the intercloud gas and a cloud around which the gas flows is a tangential discontinuity. The hydrodynamical instability of this tangential discontinuity causes the formation of a turbulent wake—a long, quasi-cylindrical or quasi-conical region of turbulent motion transported downstream from the cloud. When such a turbulent wake crosses the line of sight, observational effects associated with scattering in an interstellar plasma can arise, but the morphology and kinematics of such a scattering region are fundamentally different from the models commonly used to interpret interstellar-scintillation observations (thin phase screens or a homogeneous medium with random electron-density fluctuations). For this reason, the use of approximations based on standard models to analyze observational manifestations of scattering in turbulent wakes can lead to qualitatively incorrect results.

Since the direction of the intercloud plasma flow is close to radial, the intersection of a turbulent wake with the line of sight is possible only when the line of sight passes relatively close to direction toward the cloud responsible for the formation of the wake. In this case, the intersection of the boundary of the scattering region occurs in a direction that is close to tangential. Scintillations due to scattering on two-dimensional structures intersected almost tangentially were considered in [22], where it was shown that deviations of interface surface from a flat geometry strongly influence the observed characteristics of the scattered radiation. In particular, with such a geometry, the scattering turns out to be highly anisotropic.

Our estimate of the distance to the scattering layer derived from the drift velocity of the scintillation pattern assumed that the tangential velocity of the region responsible for the scintillations relative to the Sun was substantially lower than the tangential component of the velocity of the pulsar. This assumption may not be fulfilled in the case of scattering in a turbulent wake, leading to errors in the derived distance to the scattering screen.

9. CONCLUSION

We have presented an analysis of VLBI observations of the pulsar PSR B0833−45. We concluded based on the behavior of the amplitude of the visibility function for various baselines (Fig. 8b) that the scattering disk was elliptical, with a 2:1 axial ratio. This conclusion was supported by the behavior of the visibility-function amplitude as a function of the delay. The major axis of the elliptical scattering disk was inferred to be approximately parallel to the motion of the scintillation pattern relative to the observer.

Anisotropic scattering can be explained by the specific properties of the turbulent layers in the supernova remnant, as explained in the previous section. The formal estimates of the distance to the effective scattering screen we have obtained correspond to a screen position closer to the observer than the supernova envelope. However, we believe that this discrepancy is due to the presence of other, weaker sources of scattering located between the Sun and the shell, and it is scattering of the pulsar radio emission from turbulent layers close to the Vela supernova remnant that determines the parameters of the scattering disk.

ACKNOWLEDGMENTS

The RadioAstron project has been realized by the Astro Space Center of the Lebedev Physical Institute of the Russian Academy of Sciences and the S.A. Lavochkin Science and Production Association, under contract with the Russian Space Agency, together with many scientific and technological organizations in Russia and other countries.

This work was supported by the Russian Foundation for Basic Research (project 1602-00954), and was based on the results of observations of the Long Baseline Array interferometer, consisting of the telescopes of the Australian Telescope National Facility (Australia and the University of Tasmania) and the Hartebeesthoek Radio Observatory in South Africa.

REFERENCES

1. T. H. Hankins and B. J. Rickett, Methods Comput. Phys. **14**, 55 (1975).
2. N. S. Kardashev, V. V. Khartov, V. V. Abramov, V. Yu. Avdeev, A. V. Alakoz, Yu. A. Aleksandrov, S. Ananthakrishnan, V. V. Andreyanov, A. S. Andrianov, N. M. Antonov, M. I. Artyukhov, M. Yu. Arkhipov, W. Baan, N. G. Babakin, N. Bartel', et al., Astron. Rep. **57**, 154 (2013).
3. R. Dodson, D. Legge, J. E. Reynolds, and P. M. McCulloch, Astrophys. J. **596**, 1137 (2003).
4. E. N. Fadeev, A. S. Andrianov, M. S. Burgin, M. V. Popov, A. G. Rudnitskiy, V. I. Shishov, T. V. Smirnova, and V. A. Zuga, Mon. Not. R. Astron. Soc. **480**, 4199 (2018).
5. E. N. Fadeev, A. S. Andrianov, V. A. Zuga, M. V. Popov, A. G. Rudnitskii, T. V. Smirnova, V. A. Soglasnov, and V. I. Shishov, Izv. Krymsk. Astrofiz. Observ. **114**, 151 (2018).
6. A. G. Rudnitskii, M. V. Popov, and V. A. Soglasnov, Astron. Rep. **61**, 393 (2017).
7. D. R. Stinebring, M. A. McLaughlin, J. M. Cordes, K. M. Becker, J. E. E. Goodman, M. A. Kramer, J. L. Sheckard, and C. T. Smith, Astrophys. J. **549**, L97 (2001).
8. V. I. Shishov, T. V. Smirnova, C. R. Gwinn, A. S. Andrianov, M. V. Popov, A. G. Rudnitskiy, and V. A. Soglasnov, Mon. Not. R. Astron. Soc. **468**, 3709 (2017).
9. A. S. Andrianov, T. V. Smirnova, V. I. Shishov, C. Gwinn, and M. V. Popov, Astron. Rep. **61**, 513 (2017).
10. C. R. Gwinn, N. Bartel, and J. M. Cordes, Astrophys. J. **410**, 673 (1993).
11. R. Blandford and R. Narayan, Mon. Not. R. Astron. Soc. **213**, 591 (1985).
12. V. I. Shishov, T. V. Smirnova, W. Sieber, V. M. Malofeev, et al., Astron. Astrophys. **404**, 557 (2003).
13. T. V. Smirnova, V. I. Shishov, M. V. Popov, C. R. Gwinn, et al., Astrophys. J. **786**, 115 (2014).
14. K. M. Desai, C. R. Gwinn, J. Reynolds, E. A. King, et al., Astrophys. J. **393**, L75 (1992).
15. C. R. Gwinn, M. V. Popov, N. Bartel, A. S. Andrianov, et al., Astrophys. J. **822**, 96 (2016).
16. J. M. Cordes, B. J. Rickett, D. R. Stinebring, and W. A. Coles, Astrophys. J. **637**, 346 (2006).
17. I. Sushch, B. Hnatyk, and A. Neronov, Astron. Astrophys. **525**, A154 (2011).
18. R. J. Reynolds, Astrophys. J. **203**, 151 (1976).
19. C. R. Purcell, B. M. Gaensler, X. H. Sun, E. Carretti, et al., Astrophys. J. **804**, 22 (2015).
20. A. V. Pynzar', Astron. Rep. **61**, 417 (2017).
21. R. L. White and K. S. Long, Astrophys. J. **373**, 543 (1991).
22. U.-L. Pen and Y. Levin, Mon. Not. R. Astron. Soc. **442**, 3338 (2014).

Translated by E. Seifina